

# Parallel overlapping-domain decomposition FDFD for modeling of large-scale complex nanostructures

ZHANWEN WANG,<sup>1</sup> CHENGNIAN HUANG,<sup>1</sup> WANGTAO LU,<sup>2</sup> YUNTIAN CHEN,<sup>3,4</sup> AND WEI E. I. SHA<sup>1,5</sup> D

**Abstract:** The increasing complexity and scale of photonic and electromagnetic devices demand efficient and accurate numerical solvers. In this work, we develop a parallel overlapping domain decomposition method (DDM) based on the finite-difference frequency-domain (FDFD) formulation to model the electromagnetic response of large-scale complex nanostructures. The global computational domain is partitioned into multiple overlapping subdomains terminated with perfectly matched layers (PMLs), enabling seamless source transfer between adjacent subdomains. A sparse factorization is employed to accelerate the iterative solution process, while an OpenMP-based parallel implementation ensures high scalability. Several numerical examples are provided to validate the efficiency and accuracy of the proposed algorithm. The results demonstrate excellent agreement with analytical and commercial COMSOL solutions. Notably, the method achieves up to an order of magnitude reduction in computation time, highlighting its potential as a powerful tool for large-scale photonic and electromagnetic modeling.

© 2025 Optica Publishing Group under the terms of the Optica Open Access Publishing Agreement

#### 1. Introduction

Recent advances in electromagnetic and photonic technologies have created a pressing demand for numerical solvers capable of handling systems with extremely large scales and intricate geometries. Emerging devices—including large-scale photonic integrated circuits (PICs) [1,2], metasurface [3,4], and massive antenna arrays [5]—often involve complex geometries, multi-scale interactions, and millions to billions of degrees of freedom (DoFs). Accurate and efficient modeling of such systems is crucial for the development of applications ranging from high-speed optical interconnects to next-generation wireless communications. However, traditional full-wave solvers, such as the finite-difference time-domain (FDTD) [6] and the finite-element method (FEM) [7], face prohibitive memory and time costs when tackling large electrical sizes, multiscale features, and strong near-field coupling. For instance, large-scale photonic crystal slabs [8], diffractive optical waveguides [9–11] and metasurface-based flat lenses [12–14] often require simultaneous resolution of subwavelength features and global field distributions, leading to extremely large sparse linear systems. The increasing computational burden is becoming a major barrier for the rapid design and optimization of next-generation photonic and electromagnetic devices.

To address these challenges, several efficient strategies have been proposed. Locally periodic approximation (LPA) simplifies metasurface and metalens design by neglecting long-range coupling [15–18]. Hybrid wave–ray strategies combine rigorous full wave solvers (e.g., FDTD,

#578619 Journal © 2025 https://doi.org/10.1364/OE.578619

<sup>&</sup>lt;sup>1</sup>The College of Information Science and Electronic Engineering, Zhejiang University, Hangzhou 310027, China

<sup>&</sup>lt;sup>2</sup>The School of Mathematical Sciences, Zhejiang University, Hangzhou 310027, China

<sup>&</sup>lt;sup>3</sup>School of Optical and Electronic Information, Huazhong University of Science and Technology, Wuhan 430074, China

<sup>&</sup>lt;sup>4</sup>yuntian@hust.edu.cn

<sup>&</sup>lt;sup>5</sup>weisha@zju.edu.cn

Fourier optics, FEM) with global ray tracing (RT) propagation, enabling scalable modeling of diffractive waveguide arrays, multilayer diffractive optics, and large-area diffraction-coupled systems [19–22]. This approach preserves key wave phenomena such as diffraction, coupling, and near-field scattering, while leveraging the computational efficiency of ray methods for large-scale propagation. Despite their efficiency, these approximations inevitably sacrifice accuracy in strongly coupled or non-periodic scenarios.

Domain decomposition method (DDM) provides a powerful "divide-and-conquer" framework for large-scale electromagnetic simulations, in which the computational domain is partitioned into smaller subdomains, which can be solved independently and in parallel. Over the years, techniques such as "cement" element method [23,24], finite-element tearing and interconnecting (FETI) algorithm [25,26] and higher-order transmission conditions [27,28] have been successfully applied to the analysis of massive antenna arrays, electromagnetic bandgap structures and frequency-selective surfaces(FSS) and so on [29–32]. The Dirichlet-to-Neumann (DtN) type DDM has been employed to efficiently analyze photonic crystal devices [33,34]. More recently, Zhiming Chen introduced the source transfer domain decomposition method (STDDM) for layered media [35,36], in which sources are transferred layer by layer, enabling efficient solutions with perfectly matched layers (PML). Parallel STDDM has shown excellent performance in solving velocity models and multilayer propagation problems [37–39], but their applications have been limited to relatively simple geometries and excitations conditions.

In this paper, we extend the STDDM framework to the large-scale complex nanostructures using the finite-difference frequency-domain (FDFD) formulation. Previous STDDM studies primarily focus on mathematical convergence analysis and simple propagation models. In contrast, our approach represents a general optical implementation that supports arbitrary geometries, inhomogeneous materials, and diverse excitation types (e.g., scattering and mode sources), thus substantially broadening the applicability of STDDM in realistic electromagnetic modeling. Furthermore, unlike existing STDDM implementations that rely solely on iterative source transfer, we integrate sparse factorization [40] into the framework. Noticing the fact that only the source terms need to be modified during iterations, this factorization is introduced to reduce each iteration to an efficient matrix–vector multiplication. Moreover, we implement the proposed method with an efficient OpenMP-based parallelization strategy and systematically analyze the impact of subdomain partitioning on parallel efficiency, offering practical guidelines for large-scale simulations.

This paper is organized as follows: we introduce the overall framework and basic theory of the proposed method in Section 2. In Section 3, the efficiency and superiority of the proposed method are demonstrated through two numerical examples: the scattering of a dielectric cylinder and a large-scale trapezoidal-shaped topological optical waveguide. Finally, the conclusion is reached in section 4.

#### 2. Basic theory

# 2.1. Finite-difference equation

The FDFD method is a well-established numerical technique for solving Maxwell's equations in the frequency domain. By discretizing the computational domain using a structured grid, the partial differential equations governing electromagnetic wave propagation are transformed into large sparse linear systems. The FDFD approach is especially attractive for modeling complex materials and geometries, as it directly accommodates inhomogeneous and anisotropic media.

In two-dimensional transverse magnetic (TM) polarization, the wave equation of the total electric field  $E_z^t$  is given by:

$$\nabla \cdot \left(\frac{1}{\mu_r} \nabla E_z^t\right) + k_0^2 \varepsilon_r E_z^t = 0,\tag{1}$$

where  $\varepsilon_r$  and  $\mu_r$  represent the relative electric permittivity and magnetic permeability, respectively. In this work, we assume that  $\mu_r = 1$ .  $k_0 = \frac{2\pi}{\lambda}$  is the free-space wavenumber, where  $\lambda$  is the wavelength.

As shown in Fig. 1(a), using the notations of  $\Phi_0 = E_z^t(i,j)$ ,  $\Phi_1 = E_z^t(i-1,j)$ ,  $\Phi_2 = E_z^t(i+1,j)$ ,  $\Phi_3 = E_z^t(i,j-1)$ ,  $\Phi_4 = E_z^t(i,j+1)$ , the discretized FDFD forms for the wave equation Eq. (1) is of the form [41]

$$-2\left(\frac{1}{\Delta_x^2} + \frac{1}{\Delta_y^2}\right)\Phi_0 + k_0^2 \bar{\varepsilon}\Phi_0 + \frac{\Phi_1 + \Phi_2}{\Delta_x^2} + \frac{\Phi_3 + \Phi_4}{\Delta_y^2} = 0,\tag{2}$$

$$\bar{\varepsilon} = \frac{\varepsilon_1 + \varepsilon_2 + \varepsilon_3 + \varepsilon_4}{4},\tag{3}$$

where  $\Delta_x$  and  $\Delta_y$  are the spatial step along the *x*-direction and *y*-direction, respectively. This finite-difference equation is enforced at each interior grid node (i, j), leading to a large sparse linear system, which is solved for the field  $E_x^t$  under proper boundary conditions and source:

$$\mathbf{A}\mathbf{e} = \mathbf{b},\tag{4}$$

where  $\bf A$  is a sparse matrix with the structure of Eq. (2) on uniform grids,  $\bf e$  is the unknown total field vector and  $\bf b$  represents the discrete source term.

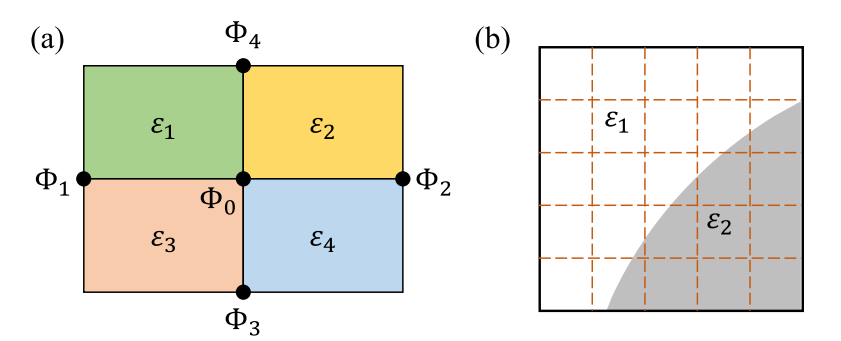


**Fig. 1.** (a) The five-point stencil for the FDFD method, where  $\Phi_0$  represents the central node and  $\Phi_1$  to  $\Phi_4$  denote adjacent nodes.  $\varepsilon$  is the relative permittivity in the discretized region. (b) The subcell method for material interfaces. The relative permittivity  $\varepsilon_1$  and  $\varepsilon_2$  are averaged across fine subcells to accurately resolve boundary effects.

For scattering problems, the total field  $E_z^t$  is decomposed into the incident field  $E_z^{inc}$  and the scattered field  $E_z^s$ :

$$E_z^t = E_z^{inc} + E_z^s, (5)$$

The incident field  $E_z^{inc}$  satisfies the wave equation in the background medium (assuming air):

$$\nabla^2 E_z^{inc} + k_0^2 E_z^{inc} = 0, \tag{6}$$

Subtracting Eq. (6) from the Eq. (1) yields a differential equation for the scattered field [42]:

$$\nabla^2 E_z^s + k_0^2 \varepsilon_r E_z^s = -k_0^2 (\varepsilon_r - 1) E_z^{inc}. \tag{7}$$

This scattered field equation can also be discretized using the same finite-difference scheme to get the form of Eq. (4) where the right-hand side contains the equivalent source term based on the incident field.

For the cells intersected by material interfaces, as illustrated in Fig. 1(b), we apply a subcell integration method to accurately compute the effective relative permittivity [6]. Each coarse grid cell is subdivided into fine subcells and then the average dielectric properties is assigned according to the number of subcells in one medium  $N_1$  as well as in the other medium  $N_2$ . Here, the medium type of each subcell is determined by the location of its center relative to the material interface:

$$\varepsilon_{ave} = \frac{\varepsilon_1 N_1 + \varepsilon_2 N_2}{N_1 + N_2},\tag{8}$$

This approach significantly improves the accuracy at curved boundaries compared to standard cell-centered assignments.

# 2.2. Perfectly matched layer

To simulate unbounded scattering problems using FDFD, it is essential to truncate the computational domain with an absorbing boundary condition. We employ the PML approach, which introduces complex coordinate stretching [43] in Maxwell's equations to absorb outgoing waves without spurious reflection.

For 2D TM polarization, the PML is implemented via a complex coordinate transformation:

$$\frac{1}{s_r(x)}\frac{\partial}{\partial x}\left(\frac{1}{s_r(x)}\frac{\partial E_z^s}{\partial x}\right) + \frac{1}{s_r(y)}\frac{\partial}{\partial y}\left(\frac{1}{s_r(y)}\frac{\partial E_z^s}{\partial y}\right) + k_0^2 \varepsilon_r E_z^s = 0,\tag{9}$$

where

$$s_r = \begin{cases} 1 + \frac{j\sigma}{\omega\varepsilon_0}, & \text{within PML} \\ 1, & \text{other} \end{cases} , \tag{10}$$

where  $\varepsilon_0$  is the permittivity of free space, and  $\omega$  is the angular frequency of the incident light. The conductivities  $\sigma(x)$  and  $\sigma(y)$  are typically chosen as a polynomial grading, given by:

$$\sigma_u = \frac{\sigma_{max}}{\Delta} \left( \frac{u - \frac{1}{2}}{L} \right)^m, \quad u = 1, 2, \dots, L,$$
(11)

$$\sigma_{u+0.5} = \frac{\sigma_{max}}{\Delta} \left(\frac{u}{L}\right)^m, \quad u = 0, 1, \dots, L,$$
(12)

where  $\Delta = \Delta_x$  or  $\Delta = \Delta_y$  for the PML layers normal to the *x* axis or *y* axis. *L* is the layer number of the PML, and *m* is the order of the polynomial. In this work, the optimized settings are set to L = 8, m = 2. The coefficient  $\sigma_{max}$  is determined based on the theoretical reflection factor under normal incidence R(0), typically satisfying [44]:

$$\sigma_{max} = \frac{(m+1)ln[R(0)]}{2\eta d},\tag{13}$$

where  $\eta = 120\pi$  is the free space wave impedance, and d is the physical depth of the PML region. This ensures that the reflection from the PML is below a specified threshold.

#### 2.3. PML-based overlapping domain decomposition method

In large-scale FDFD simulations, solving the global sparse linear system becomes increasingly expensive in terms of memory and computation. To overcome these issues, we develop an overlapping domain decomposition method that leverages the existing PML structure.

The overall procedure is illustrated in Fig. 2. Initially, the simulation data of the model are loaded. The global computational domain is then partitioned into multiple subdomains, each extended with an overlapping PML region that intersects with adjacent subdomains. A global-to-local mapping is constructed to manage data association. Each subdomain independently

assembles its local FDFD matrix and performs sparse LU factorization in parallel. In the initial step, the local system is solved using its own right-hand side as Eq. (4). In subsequent iterations, each subdomain receives the field values from the overlapping PML regions of neighboring subdomains, which are used to construct an updated equivalent source. The internal field is then recalculated using the precomputed sparse factorization. The updated PML fields are passed back to adjacent subdomains. Once convergence is reached, the global solution is assembled for postprocessing.

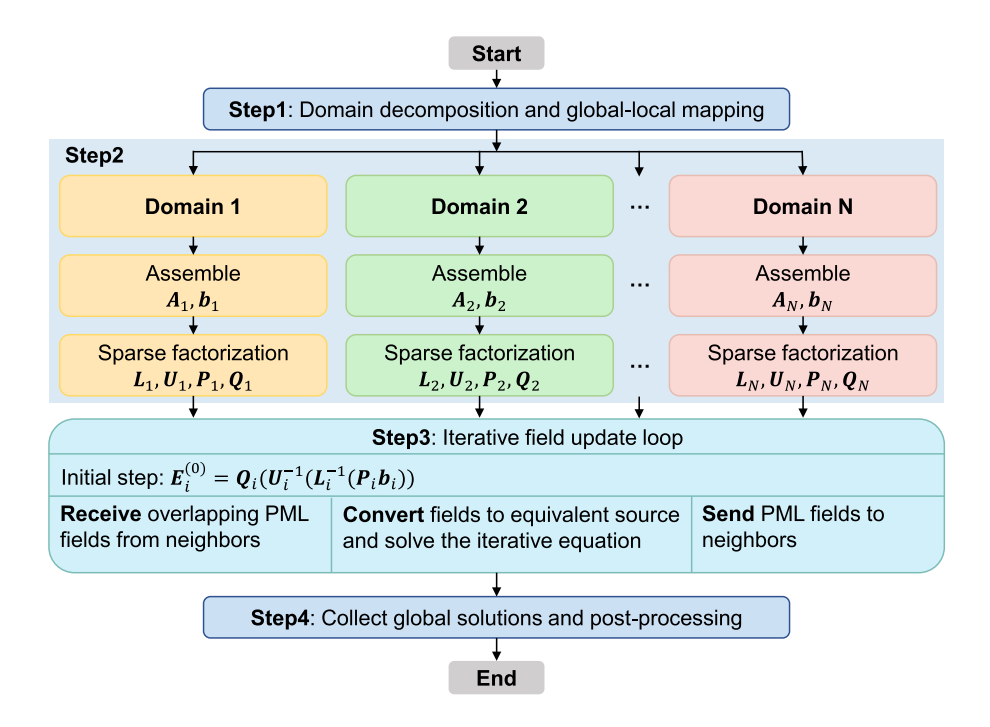


Fig. 2. The overall framework of the proposed method.

As illustrated in Fig. 3, we use the example of dividing the global computational domain  $\Omega$  into two subdomains,  $\Omega_1$  and  $\Omega_2$ , to explain the details of the proposed PML-based source transfer approach. The interior regions of the two subdomains are non-overlapping, and their union covers the entire interior of the global domain. However, as shown in Fig. 3(b) and (c), their respective PML layers extend into each other's interior regions, creating overlapping zones at the subdomain interfaces. These overlapping PML regions are the core of our method—they serve as the medium through which the equivalent sources are transferred between adjacent subdomains.

We illustrate the procedure using a representative case where a point source is located in subdomain  $\Omega_1$ , as depicted in Fig. 4, with the interface between the two subdomains indicated by a dashed line. In the initial step, each subdomain independently solves its local system using only its own source and absorbs outgoing waves through its PML layer, as described by Eqs. (4) and (9):

$$\nabla_{s}^{2} E_{i}^{(0)} + k_{0}^{2} \varepsilon_{r,i} E_{i}^{(0)} = j\omega \mu_{0} J_{i}, \quad \text{in } \Omega_{i}, \quad i = 1, 2,$$
(14)

where  $\nabla_s = \left(\frac{1}{s_x}\partial_x, \frac{1}{s_y}\partial_y\right)$  denotes the anisotropic Laplacian under complex coordinate stretching. In this example,  $J_1$  corresponds to a point source excitation, while  $J_2 = 0$ . The resulting field  $E_1^{(0)}$  is shown in Fig. 4(a).

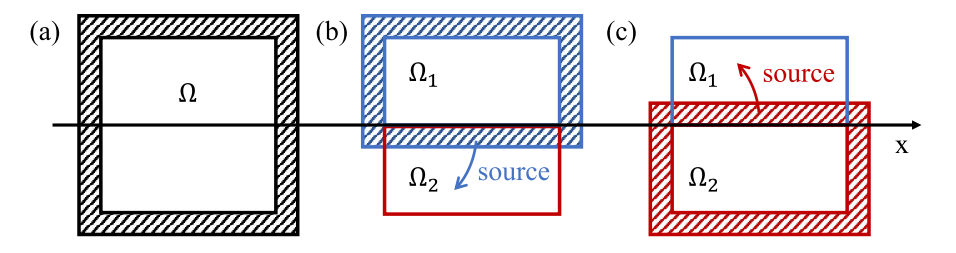


**Fig. 3.** Domain decomposition with two subdomains. The hatched area is the PML layer, the overlapping area is the source transfer region. (a) The global computational domain. (b) Subdomain  $\Omega_1$  with its local PML region. (c) Subdomain  $\Omega_2$  with its local PML region.

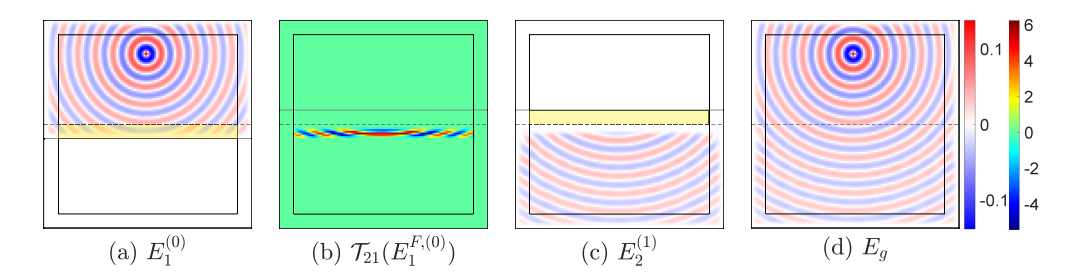


**Fig. 4.** The procedure of DDM using a point source modeling. (a) The field  $E_1^{(0)}$  of the initial step. (b) The source of  $\Omega_2$  using transfer operator  $\mathcal{T}_{21}(E_1^{F,(0)})$ . (c) The fields  $E_2^{(1)}$  of  $\Omega_2$  using the transferred source. (d) The combined global field  $E_g$ .

To facilitate source transfer, we partition the unknowns in each subdomain  $\Omega_i$  into two parts:

$$E_i = \begin{pmatrix} E_i^I \\ E_i^F \end{pmatrix},\tag{15}$$

where  $E_i^F$  denotes the electric field within the overlapping PML regions of  $\Omega_i$ , while  $E_i^I$  comprises all remaining unknowns in  $\Omega_i$ , including both the physical interior and non-overlapping PML regions. For instance, the yellow area in Fig. 4(a) highlights the overlapping region associated with  $E_i^F$ , which will later act as a transferred source to subdomain  $\Omega_2$ .

Based on Maxwell's equations for the 2D TM polarization, the equivalent electric current density of neighbor subdomain  $\Omega_p$  is given by:

$$J_{eq,p} = \frac{1}{j\omega\mu_0} \left( \nabla^2 E_i^F + k_0^2 \varepsilon_{r,p} E_i^F \right), \quad \text{in } \Omega_p,$$
 (16)

which serves as an effective source term for updating the solution in the adjacent subdomain. Notably, the equivalent source in Eq. (16) is defined using the standard Helmholtz operator, since from the perspective of  $\Omega_p$ ,  $E_i^F$  resides in its physical interior. For convenience, we define a transfer operator as:

$$\mathcal{T}_{pi}(E_i^F) = (\nabla^2 + k_0^2 \varepsilon_{r,p}) E_i^F, \tag{17}$$

where the subscript pi indicates that the field  $E_i^F$  from subdomain  $\Omega_i$  is used to compute a source term in  $\Omega_p$ . Note that the transfer operator yields a non-zero result only within the overlapping region, as visualized in Fig. 4(b).

The iterative update scheme proceeds as follows: at the *n*-th step, each subdomain solves its local equation with the transferred source term from its neighbor:

$$\nabla_s^2 E_1^{(n+1)} + k_0^2 \varepsilon_{r,1} E_1^{(n+1)} = \mathcal{T}_{12}(E_2^{F,(n)}), \quad \text{in } \Omega_1,$$
(18)

$$\nabla_s^2 E_2^{(n+1)} + k_0^2 \varepsilon_{r,2} E_2^{(n+1)} = \mathcal{T}_{21}(E_1^{F,(n)}), \quad \text{in } \Omega_2,$$
(19)

Figure 4(c) shows  $E_2^{(1)}$ , the first iteration fields in subdomain  $\Omega_2$ . In this simple one-way propagation case, the field  $E_2^{F,(1)}$  in the overlapping region is nearly zero shown in the yellow area of Fig. 4(c), indicating minimal energy reflection or backward coupling. This observation suggests rapid convergence of the iterative process. The iteration is terminated when the residual energy in the overlapping regions satisfies:

$$\sum_{i=1,2} \left\| E_i^{F,(n)} \right\| < \text{TOL} \tag{20}$$

where  $\|\cdot\|$  denotes a suitable norm (e.g., 2-norm), and TOL is a predefined convergence threshold. Finally, the global field solution is synthesized by summing all contributions from each subdomain over all iterations:

$$E_g = \sum_n (E_1^{(n)} + E_2^{(n)}). \tag{21}$$

As shown in Fig. 4(d), the resulting global solution  $E_g$  exhibits a seamless reconstruction of the total field. Notably, in the overlapping regions, the fields are naturally composed of the contributions from both subdomains (e.g.,  $E_1^{F,(0)} + E_2^{I,(1)}$ ), yet no visible discontinuity or artifact is observed, confirming the accuracy and smoothness of the decomposition-based computation. This result verifies the effectiveness of the proposed source-transfer scheme using overlapping PMLs in achieving high-fidelity domain decomposition.

To simplify the presentation and clarify the iterative mechanism, the representative example shown in Fig. 4 only places the source in subdomain  $\Omega_1$ , which leads to an alternating-update form of the iteration. However, it is important to emphasize that the proposed method is fully applicable to general scenarios where multiple subdomains contain internal sources. More complex examples involving multiple active subdomains will be presented in the next section to demonstrate this capability.

#### 2.4. Sparse factorization

In the proposed domain decomposition framework, the system matrix within each subdomain remains fixed throughout the iterative solution process, while only the right-hand side vector (i.e., the equivalent source) is updated in each iteration. This observation naturally leads to the application of the sparse factorization, which efficiently reduces computational overhead of repeated solving linear systems in the iteration by replacing direct matrix inversion with a sequence of sparse triangular factorizations and permutations. In the numerical implementation, the sparse factorization is a sparse direct solver that factors the system matrix  $\bf A$  into four components:

$$\mathbf{A} = \mathbf{P}^T \mathbf{L} \mathbf{U} \mathbf{Q}^T, \tag{22}$$

where P and Q are permutation matrices to reduce fill-in, and L and U are sparse lower- and upper-triangular matrices,respectively.

Once factorized, the system as Eq. (4) can be solved efficiently via forward and backward substitution:

$$\mathbf{e} = \mathbf{Q} \left( \mathbf{U}^{-1} \left( \mathbf{L}^{-1} \left( \mathbf{P} \mathbf{b} \right) \right) \right). \tag{23}$$

This formulation converts the expensive matrix inversion into a chain of matrix-vector multiplications, which can be efficiently executed. For a 2D FDFD discretization with N

unknowns, direct sparse solvers (e.g., sparse LU) generally incur a computational complexity of  $O(N^{1.5})$  [45]. The sparse LU factorization shares the same complexity in its initial factorization step. However, once the matrix is factorized, each subsequent triangular solve (per iteration) has a significantly lower cost of only  $O(N \log N)$  [46], as the sparse triangular factors contain only  $O(N \log N)$  non-zero entries, reducing forward/backward substitutions to efficient sparse matrix–vector multiplications. This efficiency gain becomes particularly advantageous in our framework, where multiple iterations are needed to reach convergence, and the matrix remains unchanged across iterations.

Despite its computational advantages, a well-known limitation of the sparse LU factorization is its high memory consumption, primarily caused by the fill-in implementation during matrix factorization—particularly in large-scale systems. Fortunately, this issue is effectively alleviated by our domain decomposition approach. By partitioning the global domain into smaller subdomains, the size of each local matrix  $\mathbf{A}_i$  is considerably reduced, and the corresponding factorization matrices can be stored with much lower memory cost. Therefore, the combination of domain decomposition and the sparse factorization enables efficient handling of large-scale problems with manageable memory usage, while preserving the fast convergence and numerical accuracy.

The complete solution process combining sparse factorization and domain decomposition is summarized in Algorithm 1.

Algorithm 1. Domain decomposition with N subdomains using sparse factorization.

```
1: Define:
 2: N: number of subdomains.
 3: TOL: a prescribed tolerance.
 4: 1. Preprocessing
 5: for i = 1 to N do
          Assemble local system matrix A_i and source term b_i for subdomain \Omega_i.
  7:
          Compute factorization matrices: P_i, L_i, U_i and Q_i.
 8: end for
      for i = 1 to N do
          Initialize local field: \mathbf{e}_{i}^{(0)} = \mathbf{Q}_{i} \left( \mathbf{U}_{i}^{-1} \left( \mathbf{L}_{i}^{-1} \left( \mathbf{P}_{i} \mathbf{b}_{i} \right) \right) \right)
12: 2. Iterative Solution
13: while \sum_{i} \left\| \mathbf{e}_{i}^{F,(n)} \right\| < \text{TOL do}
          for i = 1 to N do
14:
              Exchange updated fields \mathbf{e}_{j}^{F,(n-1)} from neighboring subdomains \Omega_{j}
15:
              Compute total source in subdomain \Omega_i: \mathbf{t}_i^{(n)} = \sum_j \mathcal{T}_{ij}(\mathbf{e}_j^{F,(n-1)})
Update solution: \mathbf{e}_i^{(n)} = \mathbf{Q}_i(\mathbf{U}_i^{-1}(\mathbf{L}_i^{-1}(\mathbf{P}_i\mathbf{t}_i^{(n)})))
16:
17:
          end for
18:
19:
          n \leftarrow n + 1
20: end while
21: Collect the final global field: \mathbf{e}_g = \sum_{i=1}^N \sum_n \mathbf{e}_i^{(n)}
```

#### 3. Results and discussions

In this section, we illustrate the validity, efficiency and scalability of the proposed method through two representative examples: the scattering of a dielectric cylinder and a large-scale

trapezoidal-shaped topological optical device. All examples are run on our local server, equipped with 2.60 GHz Intel Xeon Gold 6240 processor (64 cores) and 1.4 TB memory.

#### 3.1. Scattering of a dielectric cylinder

We consider the scattering of a 2D dielectric cylinder under TM and TE polarization to verify the accuracy of the proposed method. The cylinder has a radius  $r = 9\lambda_0$  and a relative permittivity of  $\varepsilon_r = 4$ . The total computational domain is  $60\lambda_0 \times 60\lambda_0$ , surrounded by PMLs of 8 grid cells in thickness. The overlapping regions between adjacent subdomains coincide with these PML layers, ensuring smooth field transition and consistent source transfer across subdomain interfaces. The incident wave frequency is 0.3 GHz, and the computational domain is discretized uniformly with 40 points per wavelength, resulting in approximately 36 million unknowns in total. The radar cross section (RCS) computed using the DDM with 64 equally partitioned subdomains (black dashed line) is compared against the analytical Mie series solution [47] (red solid line), as shown in Fig. 5(a). With the relative L2-norm errors of 3.68% for TM mode and 3.25% for TE mode RCS, the results confirm the accuracy of the proposed method.

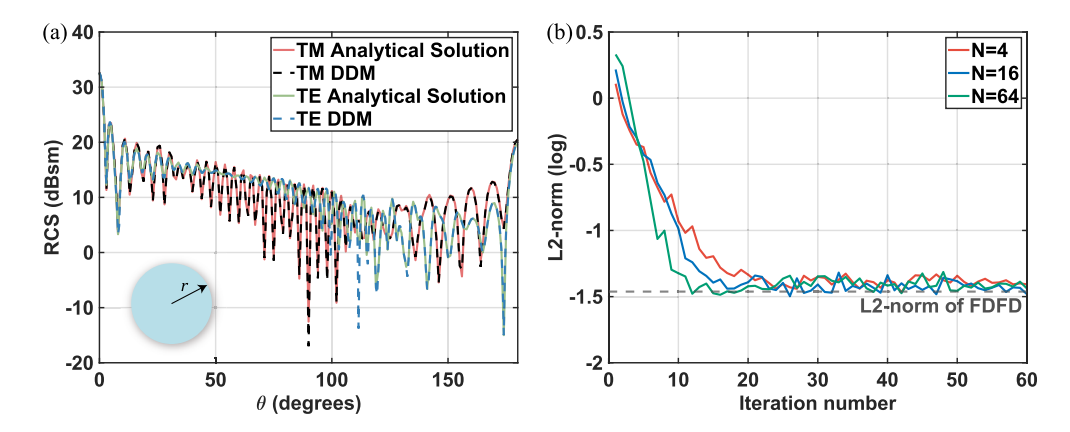


**Fig. 5.** (a) RCS of a dielectric cylinder calculated by the analytical solution and the DDM; (b) The relative L2-norm error versus iteration number for different subdomain counts.

Figure 5(b) shows the convergence behavior of the DDM in terms of the relative L2-norm error versus iteration number with respect to the analytical solution. Three configurations with different numbers of subdomains are tested: N = 4, N = 16 and N = 64. The dashed horizontal line indicates the L2-norm level of the reference FDFD solution. All cases eventually converge to a comparable accuracy level with the full-domain FDFD result, confirming the robustness and stability of the DDM. Moreover, increasing the number of subdomains significantly accelerates convergence. This behavior differs from conventional finite-element–based DDMs, where the iteration count typically grows with the number of subdomains. In the proposed method, finer domain partitioning enhances the efficiency of field exchange across interfaces. As the number of subdomains increases, a larger number of equivalent sources at internal boundaries are updated independently, yielding finer angular and directional source transfer. This mechanism effectively suppresses local field mismatches and leads to faster convergence, demonstrating the excellent scalability of the proposed method.

Table 1 summarizes the computational performance of the DDM as the number of subdomains increases. For reference, the conventional full-domain FDFD solution takes 958 seconds and consumes 102 GB of memory.

With 16 subdomains, the DDM achieves a runtime of only 101 seconds, corresponding to a speedup factor of approximately 9.5. At N = 64, the runtime further reduces to 40 seconds,

Table 1. Computational statistics of DDM with varying number of subdomains.

Number of subdomains	2	4	8	16	32	64
Unknowns per subdomain (million)	1800	900	450	225	112	56
Iterations	32	28	24	22	20	16
Time (s)	1372	495	218	101	52	40
Memory (GB)	229	180	150	122	128	136

yielding a speedup of 24× relative to the FDFD baseline. This is primarily attributed to the reduced problem size per subdomain and improved parallel efficiency, along with a decrease in the number of iterations required for convergence—which aligns with the analysis in Fig. 5(b). However, beyond 32 subdomains, the speedup approaches saturation. This is mainly due to the growing communication overhead and synchronization costs, which offsets the benefit of finer partitioning.

In terms of memory consumption, DDM requires slightly more memory than FDFD. However, this slight increase is well justified by the significant reduction in computational time, making the trade-off both acceptable and worthwhile for large-scale simulations. The increased memory usage primarily stems from the storage of sparse factorization matrices. When the number of subdomains is small, each local matrix remains large, leading to larger fill-in during factorization. As the number of subdomains increases, the size of each local matrix decreases, reducing fill-in and lowering the memory requirement. This trend results in a minimum memory usage of 122 GB at N = 16. However, when the subdomain count becomes very large (e.g., N = 64), the memory usage slightly increases again. This is due to two factors: the increased number of factorization matrices that must be stored simultaneously, and the additional communication overhead. Nevertheless, the overall memory remains within a practical range and does not hinder the scalability or efficiency of the method.

Table 2 compares the performance of the proposed DDM with a conventional Schwarz-type DDM employing first-order Robin transmission conditions [23], under the scenario where the subdomain size is fixed as  $20\lambda_0 \times 20\lambda_0$  while the number of subdomains increases. The proposed DDM exhibits significantly faster convergence than the conventional DDM, owing to its wave-propagation-based source-transfer mechanism that enables more efficient inter-subdomain coupling. As the number of subdomains increases, the total computation time of the proposed method grows only slightly, confirming its good scalability. Due to the efficient source-transfer process, the overall computation time of the proposed method is about an order of magnitude shorter than that of the conventional DDM without sparse factorization, and still maintaining a clear advantage over the factorized version.

Table 2. Comparison between the proposed DDM and the conventional Schwarz-type DDM, with and without sparse factorization, for varying numbers of subdomains.

Number of subdomains	2	4	8	16	32	64
Proposed DDM						
Iterations	18	18	20	24	25	28
Time (s)	190	194	207	218	225	244
Schwarz-type DDM						
Iterations	56	60	63	68	71	80
Time (s), without sparse factorization	2064	2185	2206	2463	2586	2834
Time (s), with sparse factorization	236	243	258	270	284	305

# 3.2. Trapezoidal-shaped topological photonic crystal waveguide

Topological photonic crystal (PhC) waveguides have attracted increasing attention in recent years owning to their inherent robustness against structural imperfections and fabrication disorder. However, their complex geometries and the demand for high numerical accuracy pose significant challenges for large-scale electromagnetic simulations. To evaluate the performance of our proposed DDM in such scenarios, we consider a trapezoidal-shaped topological PhC waveguide [48] and compare the results with the commercial software COMSOL.

The geometry of the photonic crystal and the corresponding line-defect waveguide are illustrated in the right of Fig. 6. Each unit cluster consists of six dielectric cylinders placed at the vertices of a hexagon with a side length of R=6 mm, and the lattice constant is set to a=2.8R. The cylinders have a relative permittivity  $\varepsilon_r=11.7$  and radius r=2 mm, while the defect gap width is g=21 mm. The working frequency is fixed at 7.96 GHz. Reverse orbital angular momentum (OAM) sources are applied at the upper and lower edges of the line defect, each realized by a square excitation positioned inside a hexagon near the edge. The overall structure size is approximately  $95\lambda_0 \times 20\lambda_0$  ( $\lambda_0$  is the free-space wavelength), discretized with 85 grids per  $\lambda_0$  (considering high dielectric contrast, about 25 grids per wavelength inside the dielectric). So, the total number of unknowns is 13,727,500. The entire computational domain is partitioned into 64 subdomains for the DDM simulation.

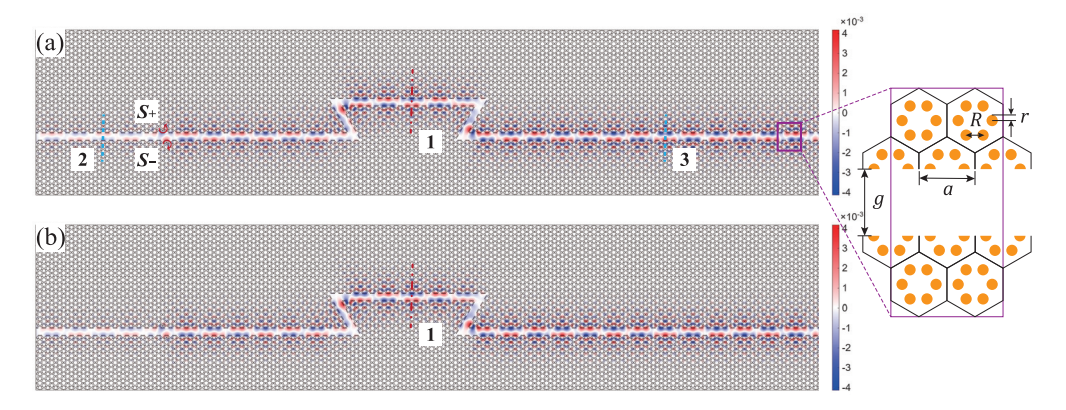


**Fig. 6.** Simulated electric field distribution and geometric structure of the topological PhC waveguide; (a) Simulation results calculated by DDM. (b) Simulation results calculated by COMSOL.

In Fig. 6, the distribution of the electric-field amplitude computed by the proposed DDM is shown, along with the results simulated by COMSOL. An excellent agreement between the two methods can be observed, indicating that our solver is capable of capturing the topological edge-state propagation accurately. To further validate the accuracy of our solver, Fig. 7 compares the normalized electric field amplitude along the reference plane 1 indicated in Fig. 6. The results obtained from DDM and COMSOL almost perfectly overlap, confirming that our approach not only reproduces the global field profile but also yields accurate field values along critical waveguide sections.

The blue dashed lines in Fig. 6(a) represent the planes used for evaluating transmitted and reflected power through  $U = 1/2 \int_{l} \text{Re}(\mathbf{E} \times \mathbf{H}^*)$ . Then, we define the backscattering ratio as  $U_2/(U_2+U_3)$  and it is calculated to be 7.9%, confirming the robustness of the topological channel even in the presence of half-cell truncation and sharp bends. Furthermore, the strong confinement of the field within the defect channel confirms that radiation leakage into the surrounding bulk photonic crystal is effectively suppressed.

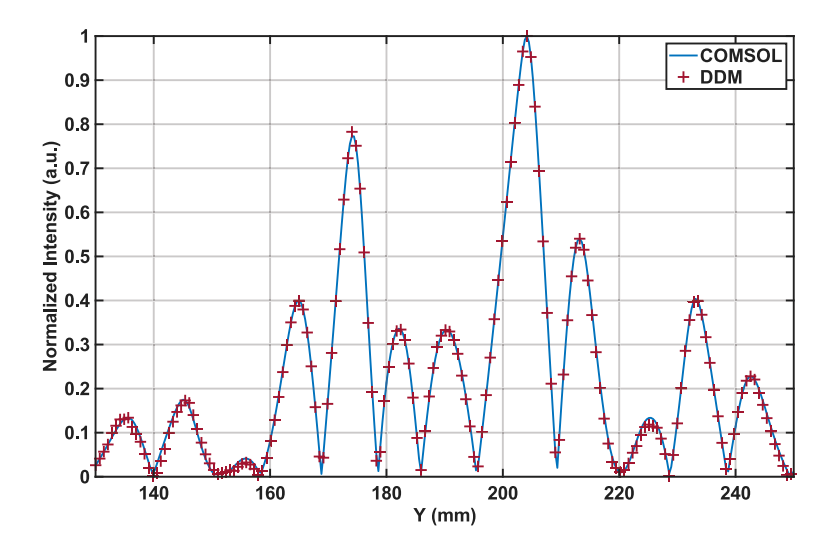


**Fig. 7.** Normalized electric field alone plane 1 in Fig. 6 by the proposed algorithm and COMSOL software.

Furthermore, Table 3 summarizes the computational performance of the different methods. Since COMSOL software is based on FEM, the comparison is carried out under comparable accuracy for fairness. The relative L2-norm errors of FDFD and DDM with respect to the COMSOL reference are 2.62% and 2.87%, respectively. In terms of computation time, DDM significantly outperforms the other two methods, completing the computation within 24 s, which corresponds to a speedup factor of approximately 13.4 compared with COMSOL and 18.3 compared with conventional FDFD. Regarding memory consumption, DDM requires 40 GB, which is moderately higher than COMSOL (23 GB) and FDFD (32 GB). The additional cost of DDM mainly originates from storing sparse factorization matrices and communication overhead, whereas COMSOL benefits from highly optimized internal memory management. Nevertheless, considering the substantial acceleration achieved by DDM, this increase in memory demand is acceptable and does not compromise overall efficiency. All corresponding codes are provided at [49].

Table 3. Computational statistics of the topological PhC waveguide.

	COMSOL	FDFD	DDM	
Computation time (s)	321	440	24	
Memory usage (GB)	23	32	40	
Relative error	_	2.62%	2.87%	

# 4. Conclusion

In this work, we have developed a parallel overlapping DDM for accelerating the calculation for large-scale complex nanostructures. By utilizing PML regions as overlapping zones for source transfer, the approach ensures consistent wave behavior, preserves physical continuity of electromagnetic fields, and enables efficient parallelization with minimal communication overhead. The incorporation of sparse factorization and OpenMP parallelization significantly achieves both numerical accuracy and computational efficiency. Compared with full-domain FDFD and commercial COMSOL software in numerical examples, the proposed approach demonstrates

substantial speedup—up to more than an order of magnitude—without compromising accuracy, at the cost of only modestly increased memory consumption. These results highlight the method's potential for addressing computational challenges in next-generation photonic integrated circuits, VR/AR devices, and other large-area electromagnetic systems. Although the present work focuses on 2D problems, the proposed overlapping-domain strategy provides a solid foundation for 3D extensions. Future efforts will integrate distributed-memory (MPI) parallelization and hierarchical solvers to enable full-vector 3D simulations of large-scale nanophotonic structures.

**Funding.** National Key Research and Development Program of China (2024YFA1012600 2023YFA1009100); National Natural Science Foundation of China (12174310); Key Project of Joint Funds for Regional Innovation and Development (U21A20425); Zhejiang Provincial NSF Distinguished Youth Program (Extended Program LRG25A010001).

**Acknowledgments.** W. L. is partially supported by the National Key Research and Development Program of China (2024YFA1012600, 2023YFA1009100), China NSF grant 12174310, and a Key Project of Joint Funds for Regional Innovation and Development (U21A20425), Zhejiang Provincial NSF Distinguished Youth Program (Extended Program LRG25A010001).

**Disclosures.** The authors declare no conflicts of interest.

**Data availability.** Data underlying the results presented in this paper are not publicly available at this time but may be obtained from the authors upon reasonable request.

#### References

- D. Yao, P. H. He, H. C. Zhang, et al., "Miniaturized photonic and microwave integrated circuits based on surface plasmon polaritons," Prog. Electromagn. Res. 175, 105–125 (2022).
- S. Ning, H. Zhu, C. Feng, et al., "Photonic-electronic integrated circuits for high-performance computing and AI accelerators," J. Lightwave Technol. 42(22), 7834–7859 (2024).
- C. Huang and W. E. I. Sha, "A parallel block preconditioner-based VIE-FFT algorithm for modeling the electromagnetic response from nanostructures," IEEE Trans. Antennas Propag. 72(1), 1051–1056 (2024).
- 4. Y. Malevich, M. S. Ergoktas, G. Bakan, *et al.*, "Very-large-scale reconfigurable intelligent surfaces for dynamic control of terahertz and millimeter waves," Nat. Commun. **16**(1), 2907 (2025).
- M. M. Taygur, I. O. Sukharevsky, and T. F. Eibert, "Investigation of massive MIMO scenarios involving rooftop propagation by bidirectional ray-tracing," Progress In Electromagnetics Research C 91, 129–142 (2019).
- 6. D. M. Sullivan, Electromagnetic Simulation using the FDTD Method (John Wiley & Sons, 2013).
- 7. J.-M. Jin, The Finite Element Method in Electromagnetics (John Wiley & Sons, 2015).
- M. Minkov, I. A. D. Williamson, L. C. Andreani, et al., "Inverse design of photonic crystals through automatic differentiation," ACS Photonics 7(7), 1729–1741 (2020).
- H. Mukawa, K. Akutsu, I. Matsumura, et al., "A full-color eyewear display using planar waveguides with reflection volume holograms," J. Soc. Info. Disp. 17(3), 185–193 (2009).
- E. L. Kramer, Q. Chao, M. Schaub, et al., "End-to-end sensor system modeling and validation for AR/VR/MR applications," in *Physics and Simulation of Optoelectronic Devices XXXI*, vol. 12415 (SPIE, 2023), pp. 182–193.
- M. J. Low, T. M. Rohith, B. Kim, et al., "Refractive-diffractive hybrid optics array: Comparative analysis of simulation and experiments," J. Opt. 24(5), 055401 (2022).
- 12. A. Arbabi, E. Arbabi, S. M. Kamali, *et al.*, "Miniature optical planar camera based on a wide-angle metasurface doublet corrected for monochromatic aberrations," Nat. Commun. **7**(1), 13682 (2016).
- Y. Su and Z. N. Chen, "A flat dual-polarized transformation-optics beamscanning luneburg lens antenna using PCB-stacked gradient index metamaterials," IEEE Trans. Antennas Propag. 66(10), 5088–5097 (2018).
- F. Ding, "A review of multifunctional optical gap-surface plasmon metasurfaces," Prog. Electromagn. Res. 174, 55–73 (2022).
- R. Pestourie, C. Pérez-Arancibia, Z. Lin, et al., "Inverse design of large-area metasurfaces," Opt. Express 26(26), 33732–33747 (2018).
- J. Skarda, R. Trivedi, L. Su, et al., "Low-overhead distribution strategy for simulation and optimization of large-area metasurfaces," npj Comput. Mater. 8(1), 78 (2022).
- X. Zu, X. Sun, W. Yan, et al., "Fast and efficient inverse design framework for multifunctional metalenses," Laser Photonics Rev. 19(3), 2400886 (2025).
- Z. Li, R. Pestourie, J.-S. Park, et al., "Inverse design enables large-scale high-performance meta-optics reshaping virtual reality," Nat. Commun. 13(1), 2409 (2022).
- 19. F. Xiao, J. Wang, Z. Xiong, et al., "Numerical approximation of slowly varying envelope in finite element electromagnetism: A ray-wave method of modeling multi-scale devices," Opt. Express 33(6), 12603–12614 (2025).
- 20. F. Wyrowski and M. Kuhn, "Introduction to field tracing," J. Mod. Opt. 58(5-6), 449–466 (2011).
- J. Wang, Z. Wang, L. Liu, et al., "Multi-scale multi-domain hybrid finite element modeling of light propagation," Electromag. Sci. 2(4), 1–10 (2024).

- Z. Lokar, B. Lipovsek, A. Razzaq, et al., "Coupled modelling approach for optimization of bifacial silicon heterojunction solar cells with multi-scale interface textures," Opt. Express 27(20), A1554

  –A1568 (2019).
- S.-C. Lee, M. N. Vouvakis, and J.-F. Lee, "A non-overlapping domain decomposition method with non-matching grids for modeling large finite antenna arrays," J. Comput. Phys. 203(1), 1–21 (2005).
- 24. M. Vouvakis, Z. Cendes, and J.-F. Lee, "A FEM domain decomposition method for photonic and electromagnetic band gap structures," IEEE Trans. Antennas Propag. **54**(2), 721–733 (2006).
- M.-F. Xue and J.-M. Jin, "Nonconformal FETI-DP methods for large-scale electromagnetic simulation," IEEE Trans. Antennas Propag. 60(9), 4291–4305 (2012).
- H.-W. Gao, M.-L. Yang, and X.-Q. Sheng, "Nonconformal FETI-DP domain decomposition methods for FE-BI-MLFMA," IEEE Trans. Antennas Propag. 64(8), 3521–3532 (2016).
- Z. Peng and J.-F. Lee, "Non-conformal domain decomposition method with mixed true second order transmission condition for solving large finite antenna arrays," IEEE Trans. Antennas Propag. 59(5), 1638–1651 (2011).
- 28. P.-H. Jia, L. Lei, J. Hu, *et al.*, "Twofold domain decomposition method for the analysis of multiscale composite structures," IEEE Trans. Antennas Propag. **67**(9), 6090–6103 (2019).
- R. Zhao, J. Hu, H. Zhao, et al., "Solving EM scattering from multiscale coated objects with integral equation domain decomposition method," Antennas Wirel. Propag. Lett. 15, 742–745 (2016).
- R. Zhao, Y. Chen, X.-M. Gu, et al., "A local coupling multitrace domain decomposition method for electromagnetic scattering from multilayered dielectric objects," IEEE Trans. Antennas Propag. 68(10), 7099–7108 (2020).
- W.-J. Wang, R. Xu, H.-Y. Li, et al., "Massively parallel simulation of large-scale electromagnetic problems using one high-performance computing scheme and domain decomposition method," IEEE Trans. Electromagn. Compat. 59(5), 1523–1531 (2017).
- 32. B. MacKie-Mason, Y. Shao, A. Greenwood, *et al.*, "Supercomputing-enabled first-principles analysis of radio wave propagation in urban environments," IEEE Trans. Antennas Propag. **66**(12), 6606–6617 (2018).
- Z. Hu and Y. Lu, "Efficient analysis of photonic crystal devices by Dirichlet-to-Neumann maps," Opt. Express 16(22), 17383–17399 (2008).
- Z. Hu and Y. Lu, "Improved Dirichlet-to-Neumann map method for modeling extended photonic crystal devices," Opt. Quantum Electron. 40(11-12), 921–932 (2008).
- Z. Chen and X. Xiang, "A source transfer domain decomposition method for Helmholtz equations in unbounded domain," SIAM J. Numer. Anal. 51(4), 2331–2356 (2013).
- 36. Z. Chen and X. Xiang, "A source transfer domain decomposition method for Helmholtz equations in unbounded domain part II: Extensions," Numerical Mathematics: Theory, Methods and Applications 6, 538–555 (2013).
- 37. W. Leng, "A fast propagation method for the Helmholtz equation," Chinese Journal of Engineering Mathematics 32, 726–742 (2015).
- W. Leng and L. Ju, "Trace transfer-based diagonal sweeping domain decomposition method for the Helmholtz equation: Algorithms and convergence analysis," J. Comput. Phys. 455, 110980 (2022).
- R. Dai, A. Modave, J.-F. Remacle, et al., "Multidirectional sweeping preconditioners with non-overlapping checkerboard domain decomposition for Helmholtz problems," J. Comput. Phys. 453, 110887 (2022).
- 40. J. Xia, S. Chandrasekaran, M. Gu, *et al.*, "Superfast multifrontal method for large structured linear systems of equations," SIAM J. Matrix Anal. Appl. **31**(3), 1382–1411 (2010).
- 41. P.-f. Qiao, W. E. I. Sha, W. C. H. Choy, *et al.*, "Systematic study of spontaneous emission in a two-dimensional arbitrary inhomogeneous environment," Phys. Rev. A **83**(4), 043824 (2011).
- 42. W. E. I. Sha, W. C. H. Choy, and W. C. Chew, "A comprehensive study for the plasmonic thin-film solar cell with periodic structure," Opt. Express 18(6), 5993–6007 (2010).
- 43. W. C. Chew, J. M. Jin, and E. Michielssen, "Complex coordinate stretching as a generalized absorbing boundary condition," Microw. Opt. Technol. Lett. 15(6), 363–369 (1997).
- J.-P. Berenger, "Three-dimensional perfectly matched layer for the absorption of electromagnetic waves," J. Comput. Phys. 127(2), 363–379 (1996).
- R. J. Lipton, D. J. Rose, and R. E. Tarjan, "Generalized nested dissection," SIAM J. Numer. Anal. 16(2), 346–358 (1979).
- 46. S. Wang, X. S. Li, F.-H. Rouet, *et al.*, "A parallel geometric multifrontal solver using hierarchically semiseparable structure," ACM Trans. Math. Softw. **42**(3), 1–21 (2016).
- 47. J. A. Kong, Electromagnetic Wave Theory (Wiley, 1986).
- 48. M. L. N. Chen, L. J. Jiang, Z. Lan, *et al.*, "Pseudospin-polarized topological line defects in dielectric photonic crystals," IEEE Trans. Antennas Propag. **68**(1), 609–613 (2020).
- Z. Wang, "Code repository for the proposed domain decomposition method," Github, 2025, https://github.com/qqot/STDDM2d.git.